CL-160419 Received: April 26, 2016 | Accepted: June 4, 2016 | Web Released: June 11, 2016

Preferential Facet Growth of Methylammonium Lead Halide Single Crystals Promoted by Halide Coordination

Yi Zhang,[1,2] Fuqiang Huang,[1,2] and Qixi Mi*[2]
[1]*Shanghai Institute of Ceramics, Chinese Academy of Sciences, Shanghai 200050, P. R. China*
[2]*School of Physical Science and Technology, ShanghaiTech University, Shanghai 201210, P. R. China*

(E-mail: miqx@shanghaitech.edu.cn)

Perovskite solar cells utilize solution-processed $CH_3NH_3PbI_3$ thin films as the active layer material, whose morphology and exposed facets directly contribute to the device efficiency and stability. We investigated various conditions for growing $CH_3NH_3PbX_3$ (X = Br, I) crystals from solutions, and found that bromide, nonaqueous solvents, and higher X^-/PbX_2 ratios favor the growth of cuboids over dodecahedra. We propose that these factors promote the coordination of X^- to Pb^{2+} on the growing surfaces, thus making the $\{110\}_c$ faces outgrow the $\{100\}_c$ faces.

Keywords: Perovskite solar cell | Crystal facet growth | Dodecahedra and cuboid

Organic–inorganic hybrid perovskites represented by $MAPbX_3$ (MA: methylammoniun, X = Br, I) exhibit many excellent semiconducting properties that are beneficial to optoelectronic and photonic applications.[1–3] In particular, the power conversion efficiency of perovskite solar cells (PSCs) has increased from 3.8%[4] to 22.1%[5] within seven years. Besides impressive efficiencies, the solution processability of perovskites significantly reduces the costs of large-scale production, compared with conventional semiconductors such as Si and GaAs. A key factor for further enhancing the performance and stability of PSCs is morphology control of the $MAPbX_3$ thin films. Although a variety of fabrication techniques, including two-step spin-coating,[6] hot casting,[7] and intramolecular exchange,[8] have been developed to achieve high device performances, relatively less is known about how different fabrication conditions affect the morphology and texture of the as-prepared $MAPbX_3$ films.

Theoretical calculations[9] suggest that cuboid $MAPbI_3$ crystallites bearing the rectangular (110) and (001) faces are more advantageous for charge carrier diffusion and collection than other exposed faces. However, solution-grown $MAPbI_3$ single crystals are found in most reports[10–13] as dodecahedra featuring rhombic (100) and (112) facets, although $MAPbBr_3$ single crystals are usually cuboid.[12–15] This apparent discrepancy between the preferred and actual morphologies of $MAPbI_3$ prompted us to find factors that favor the growth of cuboid $MAPbI_3$ single crystals. We also wanted to identify a unified mechanism to explain why $MAPbBr_3$ and $MAPbI_3$ usually exhibit distinct crystal morphologies although the two perovskites are nearly isostructural.

For growing $MAPbX_3$ single crystals, we employed three methods depending on the nature of the solvent; Table 1 lists the experimental conditions in detail. Slow cooling of saturated solutions of $MAPbX_3$ in the corresponding aqueous hydrohalic acid[16] afforded dodecahedral crystals for both X = Br and I (Figures 1A and 1D). On the other hand, oversaturation of a 1:1 mixture of MABr and $PbBr_2$ in *N*,*N*-dimethylformamide (DMF) (Figure 1B), regardless of whether induced by a rise in temperature or by vapor diffusion of chloroform (CF) as an antisolvent, consistently yielded cuboid $MAPbBr_3$ crystals (Figure 1C).

Table 1. Growth conditions for $MAPbX_3$ (X = Br, I) single crystals and resulting crystal morphologies

Entry	X^-:PbX_2	Solvent[a,b]	Temp.[a]/°C	Morphology
X = Br				
1	>20	40% aq. HBr	95 → 35	Dodecahedral
2	1	DMF	20 → 85	Cuboid
3	1	CF → DMF	40	Cuboid
X = I				
4	>10	45% aq. HI	95 → 35	Dodecahedral
5	1	GBL	20 → 135	Dodecahedral
6	1	CF → GBL	40	Irregular + PbI_2
7	2	GBL	20 → 135	Cuboid
8	3	CF → GBL	40	Cuboid

[a]An arrow in the "solvent" (for antisolvent diffusion) or "temp." (for temperature change) column indicates the driving force of crystallization. [b]DMF: *N*,*N*-dimethylformamide, GBL: γ-butyrolactone, CF: chloroform.

$MAPbI_3$ from organic solvents, however, exhibited mixed crystal morphologies. In typical processes of inverse temperature crystallization[12] (ITC) for $MAPbI_3$, dodecahedral or cuboid $MAPbI_3$ crystals several mm in size appeared from hot γ-butyrolactone (GBL) solutions within 3–5 h (see Supporting Information, Movie 1 and Movie 2). A 1:1 solution mixture of MAI and PbI_2 at 135 °C yielded dodecahedra displaying *rhombic* facets obvious to the naked eye (Figure 1E). A 2:1 starting solution produced cuboid crystals with *rectangular* facets at 135 °C but irregular shapes at 120 °C. Antisolvent vapor-assisted crystallization[14,17] (AVC) experiments at 40 °C revealed a similar trend. Thus, a 3:1 solution mixture of MAI and PbI_2 in GBL, or a 2:1:1 mixture of TBAI (TBA: tetrabutylammonium), MAI, and PbI_2, was allowed to slowly absorb CF vapor, and cuboid $MAPbI_3$ crystals appeared over a period of five days (Figure 1F), but a 1:1 solution mixture of MAI and PbI_2 in GBL gave rise to irregular black crystals along with yellow PbI_2.

The powder X-ray diffraction (XRD) patterns of ground $MAPbX_3$ crystals (Figure 2, black curves) confirm that the $MAPbBr_3$ is an ideal cubic perovskite, whereas the crystal structure of $MAPbI_3$ belongs to the tetragonal *I*4*cm* space group, regardless of the growth method and crystal morphology. For $MAPbI_3$, typical lattice parameters $a = 8.877(1)$ Å and $c = 12.672(2)$ Å with an approximate relationship $c/a = 1.428 \approx \sqrt{2}$ suggest that the crystal system deviates only slightly from the cubic symmetry. By letting an X-ray beam diffract off a crystal's top flat facet, distinct 2θ scans were obtained from the dodecahedral and cuboid $MAPbX_3$ single crystals. The blue curves in Figure 2 show that the rectangular facets of $MAPbX_3$ diffract only at ca. 14° and its

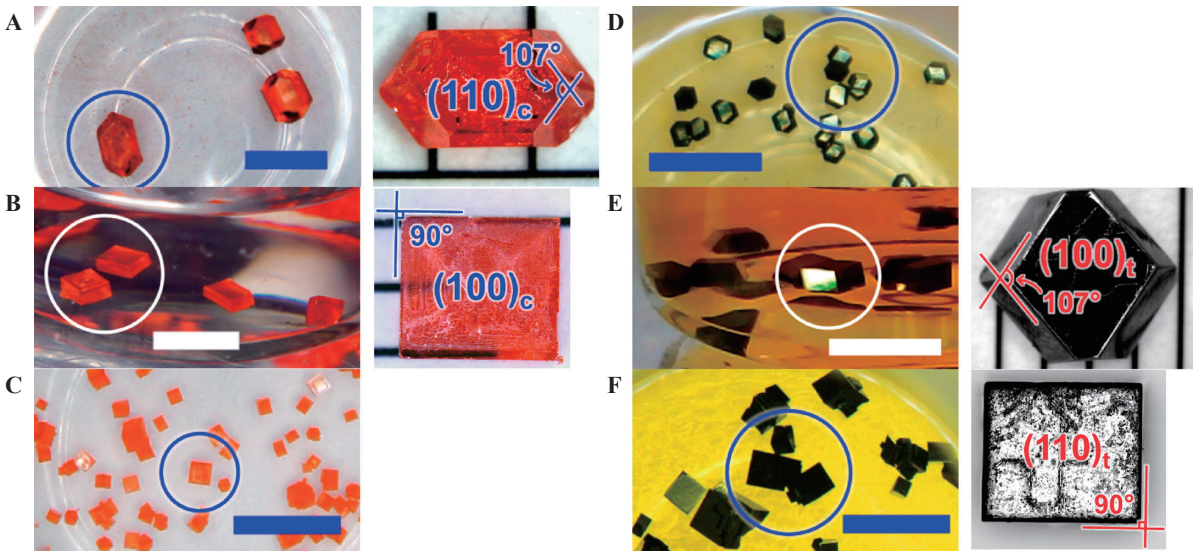

Figure 1. Photographs of $MAPbX_3$ single crystals of different morphologies (X = Br for left column and I for right column). (A, D) Dodecahedral $MAPbX_3$ from slowly-cooled aqueous HX. (B, E) Cuboid $MAPbBr_3$ and dodecahedral $MAPbI_3$ from hot organic solutions of 1:1 MAX and PbX_2. (C, F) Cuboid $MAPbX_3$ from antisolvent diffusion. Panels A–F correspond to Entries 1, 2, 3, 4, 5, and 8 of Table 1, respectively. Scale bar: 5 mm; rulings: 1 mm.

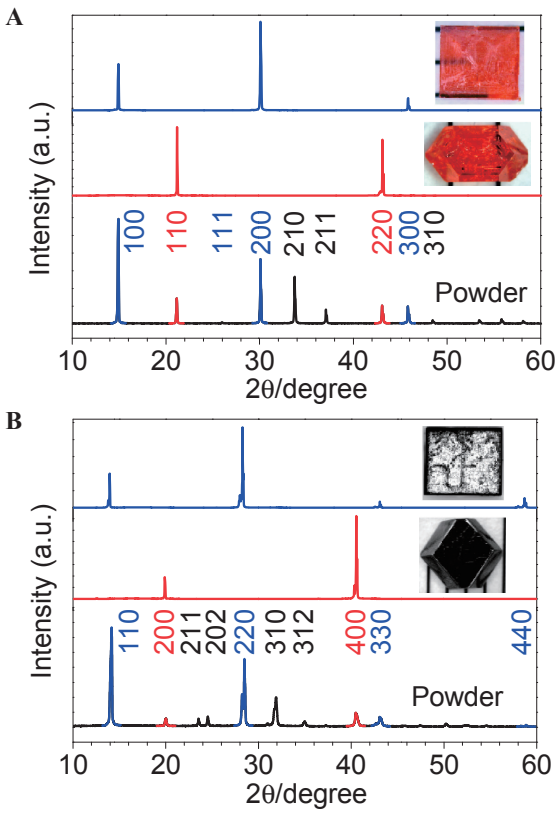

Figure 2. X-ray diffraction (XRD) patterns of (A) $MAPbBr_3$ and (B) $MAPbI_3$. Black curves: Ground $MAPbBr_3$ crystals exhibit a powder pattern of the cubic $Pm\bar{3}m$ space group, and $MAPbI_3$ powder belongs to the tetragonal $I4cm$ space group. Red curves: 2θ scans off the rhombic facet of dodecahedral $MAPbX_3$ single crystals. Blue curves: 2θ scans off the rectangular facet of cuboid $MAPbX_3$ single crystals.

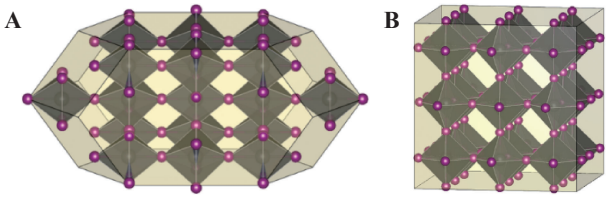

Figure 3. Atomistic model of (A) dodecahedral and (B) cuboid crystallites of $MAPbI_3$.

multiples, which are indexed to $k00$ in the cubic crystal system and to $kk0$ ($k = 1, 2, 3, \ldots$) in the tetragonal system, indicating that the rectangular facet of $MAPbBr_3$ is the $(100)_c$ surface, whereas that of $MAPbI_3$ is the $(110)_t$ surface. Hereafter, the subscripts c and t of the Miller indices denote the cubic and tetragonal crystal systems, respectively. Likewise, the rhombic facet of $MAPbBr_3$ is designated as the $(110)_c$ surface and that of $MAPbI_3$ as the $(100)_t$ surface.

Figure 3 depicts atomistic models of dodecahedral and cuboid $MAPbI_3$ crystallites. The dodecahedral model (Figure 3A) is enclosed by four $\{100\}_t$ faces that take the shape of truncated rhombus, in addition to eight rhombic $\{112\}_t$ faces. All these surfaces are nearly equivalent due to the almost cubic crystal symmetry of $MAPbI_3$ and feature a calculated obtuse angle of ca. 109°, which agrees with the actual shape and angle (107°) of the dodecahedral single crystal in Figure 1E. The cuboid model (Figure 3B) consists of nearly equivalent $\{110\}_t$ and $\{001\}_t$ faces that intersect with each other at right angles, also consistent with the cuboid in Figure 1F.

$MAPbBr_3$ is stable in the cubic phase above −37 °C,[18] but $MAPbI_3$ undergoes a second-order phase transition from the tetragonal to cubic phase at 54 °C,[19] lower than or close to the temperatures for crystal growth in Table 1. Consequently, indexing the natural facets of $MAPbI_3$ to the cubic system properly reflects the surface structures during crystal growth, and also simplifies our analysis for the growth mechanism.

Table 2. Logarithm of cumulative formation constants of PbX_3^- and PbX_4^{2-} (X = Br, I) in water and DMF

Solvent	$\log\beta(PbBr_3^-)$	$\log\beta(PbBr_4^{2-})$	$\log\beta(PbI_3^-)$	$\log\beta(PbI_4^{2-})$	Ref.
H_2O	2.54	2.04	3.14	4.43	20
DMF	12.4	13.2	9.4	10.3	21

In the Supporting Information, we have derived the equations for conversion between tetragonal indices $h_t k_t l_t$ and cubic indices $h_c k_c l_c$: $h_t = h_c - k_c$, $k_t = h_c + k_c$, and $l_t = 2l_c$. Therefore, the rhombic $(100)_t$ and $(112)_t$ planes in the tetragonal phase become $(110)_c$ and $(101)_c$, which belong to the equivalent family of $\{110\}_c$ planes in the cubic crystal system, whereas the rectangular planes $(110)_t$ and $(002)_t$ in the tetragonal phase translate to the cubic $\{100\}_c$ planes. Note that the two plane families $\{100\}_c$ and $\{110\}_c$ do not have any member in common.

We propose a mechanism based on halide coordination to interpret the above experimental phenomena, which obey the general trend that bromide, nonaqueous solvents, and higher X^-/PbX_2 ratios favor the growth of cuboid single crystals with rectangular $\{100\}_c$ facets.

Pb^{2+} coordinates with halide X^- (X = Cl, Br, and I) in both water and nonaqueous solvents, and PbX_3^- and PbX_4^{2-} are the two complexes most intensively investigated. Table 2 shows the cumulative formation constants β_3 and β_4 in *N*,*N*-dimethylformamide (DMF) are orders of magnitudes higher than those in water. Moreover, $PbBr_3^-$ and $PbBr_4^{2-}$ are more stable than their iodo counterparts in DMF. Due to lack of experimental β values in GBL, we assume that PbX_3^- and PbX_4^{2-} in GBL should exhibit the same order of relative stability as in DMF, because DMF and GBL are both polar aprotic solvents with very similar dielectric constants ($\varepsilon = 38.25$ and 39.0, respectively[22]).

The stability constants of PbX_3^- and PbX_4^{2-} reflect the affinity of X^- toward Pb^{2+} in solution and at the interface between crystal and mother liquor, which follows the order $Br^- \rightarrow Pb^{2+}$ in DMF > $I^- \rightarrow Pb^{2+}$ in DMF > Br^-, $I^- \rightarrow Pb^{2+}$ in H_2O. This relation unifies our experimental results under various conditions, and suggests that an appropriate combination of solvent, halide, and X^-/PbX_2 ratio that favors coordination of X^- to $MAPbX_3$ surfaces will also favor the growth of rectangular $\{100\}_c$ surfaces over rhombic $\{110\}_c$ surfaces. Increasing the I^-:PbI_2 ratio without adding MA^+ had the same effect. Quantitative study of interfacial Pb–X coordination under actual growth conditions is challenging both experimentally and computationally, because of the ion–solvent interactions and net charges on the crystal surfaces.

The morphology and natural facets of the as-grown crystals is a result of the competing growth of the $\{100\}_c$ and $\{110\}_c$ facets. The number density of X^- on the $\{100\}_c$ surface equals $1/a^2$ and that on the $\{110\}_c$ surface is $\sqrt{2}/a^2$, where a is the lattice parameter in the cubic phase. Conditions that promote surface coordination of X^- are likely to preferentially accelerate the growth of more crowded $\{110\}_c$ surface over $\{100\}_c$ surface, and the latter becomes eventually visible on the macroscopic level.

To summarize, we synthesized both dodecahedral and cuboidal single crystals of $MAPbX_3$ (X = Br, I) using three methods under various conditions. From XRD and geometry measurements of mm-sized crystal facets, we indexed the rhombic and rectangular faces of $MAPbX_3$ to $\{110\}_c$ and $\{100\}_c$ in the cubic crystal system, respectively. Based on the known Pb(II)–X coordination chemistry and our experimental observations that bromide, nonaqueous solvents, and higher X^-/PbX_2 ratios favor the growth of cuboid $MAPbX_3$ crystals, we propose an atomistic model involving stronger coordination between Pb^{2+} and X^- makes the more crowded $\{110\}_c$ faces outgrow the $\{100\}_c$ faces and eventually exposes the latter. The capability to control the crystal morphology of solution-grown $MAPbX_3$ will help fabricate $MAPbX_3$ thin films with less mismatched grain boundaries and higher interfacial stability than randomly-shaped polycrystals.

This work is financially supported by a start-up funding from ShanghaiTech University, and by a research grant (No. 21403141) from the National Science Foundation of China.

Supporting Information is available on http://dx.doi.org/10.1246/cl.160419.

References and Notes

1 T. Miyasaka, *Chem. Lett.* **2015**, *44*, 720.
2 T. M. Brenner, D. A. Egger, L. Kronik, G. Hodes, D. Cahen, *Nat. Rev. Mater.* **2016**, *1*, 15007.
3 J. Berry, T. Buonassisi, D. A. Egger, G. Hodes, L. Kronik, Y.-L. Loo, I. Lubomirsky, S. R. Marder, Y. Mastai, J. S. Miller, D. B. Mitzi, Y. Paz, A. M. Rappe, I. Riess, B. Rybtchinski, O. Stafsudd, V. Stevanovic, M. F. Toney, D. Zitoun, A. Kahn, D. Ginley, D. Cahen, *Adv. Mater.* **2015**, *27*, 5102.
4 A. Kojima, K. Teshima, Y. Shirai, T. Miyasaka, *J. Am. Chem. Soc.* **2009**, *131*, 6050.
5 NREL National Center for Photovoltaics, homepage, Best Research-cell Efficiencies, http://www.nrel.gov/ncpv/images/efficiency_chart.jpg. April 22, **2016**.
6 J.-H. Im, I.-H. Jang, N. Pellet, M. Grätzel, N.-G. Park, *Nat. Nanotechnol.* **2014**, *9*, 927.
7 W. Nie, H. Tsai, R. Asadpour, J.-C. Blancon, A. J. Neukirch, G. Gupta, J. J. Crochet, M. Chhowalla, S. Tretiak, M. A. Alam, H.-L. Wang, A. D. Mohite, *Science* **2015**, *347*, 522.
8 W. S. Yang, J. H. Noh, N. J. Jeon, Y. C. Kim, S. Ryu, J. Seo, S. I. Seok, *Science* **2015**, *348*, 1234.
9 J. Haruyama, K. Sodeyama, L. Han, Y. Tateyama, *J. Phys. Chem. Lett.* **2014**, *5*, 2903.
10 Y. Dang, Y. Liu, Y. Sun, D. Yuan, X. Liu, W. Lu, G. Liu, H. Xia, X. Tao, *CrystEngComm* **2015**, *17*, 665.
11 Q. Dong, Y. Fang, Y. Shao, P. Mulligan, J. Qiu, L. Cao, J. Huang, *Science* **2015**, *347*, 967.
12 M. I. Saidaminov, A. L. Abdelhady, B. Murali, E. Alarousu, V. M. Burlakov, W. Peng, I. Dursun, L. Wang, Y. He, G. Maculan, A. Goriely, T. Wu, O. F. Mohammed, O. M. Bakr, *Nat. Commun.* **2015**, *6*, 7586.
13 Y. Liu, Z. Yang, D. Cui, X. Ren, J. Sun, X. Liu, J. Zhang, Q. Wei, H. Fan, F. Yu, X. Zhang, C. Zhao, S. Liu, *Adv. Mater.* **2015**, *27*, 5176.
14 D. Shi, V. Adinolfi, R. Comin, M. Yuan, E. Alarousu, A. Buin, Y. Chen, S. Hoogland, A. Rothenberger, K. Katsiev, Y. Losovyj, X. Zhang, P. A. Dowben, O. F. Mohammed, E. H. Sargent, O. M. Bakr, *Science* **2015**, *347*, 519.
15 Y. Fang, Q. Dong, Y. Shao, Y. Yuan, J. Huang, *Nat. Photonics* **2015**, *9*, 679.
16 J. Su, D. P. Chen, C. T. Lin, *J. Cryst. Growth* **2015**, *422*, 75.
17 D. Shi, X. Qin, Y. Li, Y. He, C. Zhong, J. Pan, H. Dong, W. Xu, T. Li, W. Hu, J.-L. Brédas, O. M. Bakr, *Sci. Adv.* **2016**, *2*, e1501491.
18 N. Onoda-Yamamuro, O. Yamamuro, T. Matsuo, H. Suga, *J. Phys. Chem. Solids* **1992**, *53*, 277.
19 M. T. Weller, O. J. Weber, P. F. Henry, A. M. Di Pumpo, T. C. Hansen, *Chem. Commun.* **2015**, *51*, 4180.
20 H. L. Clever, F. J. Johnston, *J. Phys. Chem. Ref. Data* **1980**, *9*, 751.
21 N. Matsuura, M. Takizawa, Y. Sasaki, *Nippon Kagaku Kaishi* **1976**, 1495.
22 C. Wohlfarth, in *CRC Handbook of Chemistry and Physics*, 84th ed., ed. by D. R. Lide, CRC Press, Boca Raton, **2003**, pp. 153–175.